PHYSICAL REVIEW E **83**, 041103 (2011)

Harmonic oscillator in heat bath: Exact simulation of time-lapse-recorded data and exact analytical benchmark statistics

Simon F. Nørrelykke
Department of Molecular Biology, Princeton University, Princeton, New Jersey, USA

Henrik Flyvbjerg
Department of Micro- and Nanotechnology, Technical University of Denmark, Kongens Lyngby, Denmark

(Received 2 September 2010; revised manuscript received 2 February 2011; published 4 April 2011)

The stochastic dynamics of the damped harmonic oscillator in a heat bath is simulated with an algorithm that is exact for time steps of arbitrary size. Exact analytical results are given for correlation functions and power spectra in the form they acquire when computed from experimental time-lapse recordings. Three applications are discussed: (i) The effects of finite sampling rate and time, described exactly here, are similar for other stochastic dynamical systems—e.g., motile microorganisms and their time-lapse-recorded trajectories. (ii) The same statistics is satisfied by any experimental system to the extent that it is interpreted as a damped harmonic oscillator at finite temperature—such as an AFM cantilever. (iii) Three other models of fundamental interest are limiting cases of the damped harmonic oscillator at finite temperature; it consequently bridges their differences and describes the effects of finite sampling rate and sampling time for these models as well.

DOI: 10.1103/PhysRevE.83.041103 PACS number(s): 05.40.Jc

I. INTRODUCTION

The damped harmonic oscillator in a heat bath is the archetypical bounded Brownian dynamical system with inertia and the simplest possible of this kind. Analytically solvable, it offers insights that are valid also for more complex systems. Its experimental correlation functions and power spectra are given analytically here in the form they take when computed from time-lapse-recorded trajectories. Such trajectories are generated and analyzed for illustration in an exact Monte Carlo simulation. The results differ significantly from those derived from the standard continuous-sampling formulation.

In mathematical terms, it is the Ornstein-Uhlenbeck (OU) process in a Hookean force field that we treat, and the results discussed here extend the ones given in [1,2] as well as the free case treated by Gillespie [3]. Three classical papers on the OU process are [4–6]. Historically, the model was prompted by a question by Smoluchowski regarding how inertia might modify Einstein's theory of Brownian motion [7]. Lorentz soon after pointed out that Ornstein's answer to that question was insufficient for the case of classical Brownian motion, i.e., in a fluid of density similar to the Brownian particle [8]: Hydrodynamical effects, entrainment and backflow, were more important with the time resolution that was available in the first century of Brownian motion. Inertia in classical Brownian motion became experimentally relevant only with precision calibration of optical tweezers [9,10] and was directly observed only in 2005 [11,12].

The OU process remained and remains, however, an important model for Brownian motion dominated by inertia, such as massive particles [13–15] or AFM cantilevers [16] in air, and for other kinds of persistent random motion, e.g., cell migration [17–24] and commodity pricing [25]. Consequently, the treatment given here of its experimental statistics for time-lapse-recorded data should be useful in several ways:

(i) All experimental statistics contain effects of finite sampling rate, finite sampling time, and finite statistics. They do so to various degrees, but the effects are inherent in measurements. We give exact analytical expressions for these effects, for the model treated here. Statistics for more complex systems contain the same effects qualitatively, and quantitatively as well, by degrees that we estimate.

(ii) The statistics we describe below must be found for any experimental system to the extent that system is interpreted as a damped harmonic oscillator at finite temperature—e.g., an AFM cantilever to be calibrated by interpretation of its thermal power spectrum.

(iii) Three other models are limiting cases of the model treated here:

(1) At *vanishing mass*, Einstein's theory for Brownian motion in a harmonic trap, which, e.g., is a minimal model for the Brownian dynamics of a microsphere held in an optical trap, with magnetic tweezers [26], or surface tethered by DNA [27].

(2) At *vanishing external force*, the Ornstein-Uhlenbeck model of free Brownian motion with inertia, which, e.g., is a minimal model for the persistent random motion seen in trajectories of motile cells.

(3) At *vanishing mass and external force*, Einstein's original theory for Brownian motion in a fluid at rest.

The results for the harmonic oscillator, given below, carry over to these three models. The limits are not all obvious, but always enlightening, hence described below.

(iv) As the model treated here bridges the differences between the three limiting cases, the material presented here is well suited for a pedagogical, hands-on, computer-based introduction to the four dynamic systems covered here: free/bound diffusion, with/without inertia, their equilibrium behavior, correlations, and power spectra, and their transient behavior to equilibrium.

©2011 American Physical Society

II. EXACT DISCRETIZED EINSTEIN-ORNSTEIN-UHLENBECK THEORY OF BROWNIAN MOTION IN HOOKEAN FORCE FIELD

The Einstein-Ornstein-Uhlenbeck theory for the Brownian motion of a damped harmonic oscillator in one dimension is simply Newton's second law for the oscillator with a thermal driving force, a.k.a. the Langevin equation for this system,

$$m\ddot{x}(t) + \gamma\dot{x}(t) + \kappa x(t) = F_{\text{therm}}(t), \tag{1}$$

$$F_{\text{therm}}(t) = (2k_B T\gamma)^{1/2}\eta(t). \tag{2}$$

Here $x(t)$ is the coordinate of the oscillator as function of time t, m is its inertial mass, γ is its friction coefficient, κ is Hooke's constant, and F_{therm} is the thermal force on the oscillator. Equation (2) gives the amplitude of this thermal noise explicitly in terms of γ, the Boltzmann energy $k_B T$, and $\eta(t)$, which is a normalized white-noise process, i.e., the time derivative of a Wiener process, $\eta = dW/dt$, hence

$$\langle\eta(t)\rangle = 0; \langle\eta(t)\eta(t)\rangle = \delta(t-t') \quad \text{for all} \quad t,t'. \tag{3}$$

Equation (1) can be rewritten as two coupled first-order differential equations,

$$\frac{d}{dt}\begin{pmatrix} x(t) \\ v(t) \end{pmatrix} = -\mathbf{M}\begin{pmatrix} x(t) \\ v(t) \end{pmatrix} + \frac{\sqrt{2D}}{\tau}\begin{pmatrix} 0 \\ \eta(t) \end{pmatrix}, \tag{4}$$

where we have introduced Einstein's relation $D = k_B T/\gamma$ and the 2×2 matrix

$$\mathbf{M} = \begin{pmatrix} 0 & -1 \\ \frac{\kappa}{m} & \frac{\gamma}{m} \end{pmatrix} = \begin{pmatrix} 0 & -1 \\ \omega_0^2 & \frac{1}{\tau} \end{pmatrix}. \tag{5}$$

Here $\omega_0 = \sqrt{\kappa/m}$ is the cyclic frequency of the undamped oscillator, and $\tau = m/\gamma$ is the characteristic time of the exponential decrease with time that the momentum of the particle undergoes in the absence of all but friction forces. Below, we shall also need the cyclic frequency of the damped oscillator, $\omega = \sqrt{\kappa/m - \gamma^2/(4m^2)} = \sqrt{\omega_0^2 - 1/(4\tau^2)}$, which is real for less than critical damping, $\gamma^2 < 4m\kappa$.

Equation (4) is solved by

$$\begin{pmatrix} x(t) \\ v(t) \end{pmatrix} = \frac{\sqrt{2D}}{\tau}\int_{-\infty}^{t} dt'\, e^{-\mathbf{M}(t-t')}\begin{pmatrix} 0 \\ \eta(t') \end{pmatrix}, \tag{6}$$

which, for arbitrary positive Δt and with $t_j = j\Delta t, x_j = x(t_j)$, and $v_j = v(t_j)$, gives us the recursive relation

$$\begin{pmatrix} x_{j+1} \\ v_{j+1} \end{pmatrix} = e^{-\mathbf{M}\Delta t}\begin{pmatrix} x_j \\ v_j \end{pmatrix} + \begin{pmatrix} \Delta x_j \\ \Delta v_j \end{pmatrix}, \tag{7}$$

where

$$\begin{pmatrix} \Delta x_j \\ \Delta v_j \end{pmatrix} = \frac{\sqrt{2D}}{\tau}\int_{t_j}^{t_j+\Delta t} dt'\, e^{-\mathbf{M}(t_j+\Delta t-t')}\begin{pmatrix} 0 \\ \eta(t') \end{pmatrix} \tag{8}$$

and the time-independent matrix exponential can be written

$$e^{-\mathbf{M}\Delta t} = e^{-\frac{\Delta t}{2\tau}}\,[\cos(\omega\Delta t)\mathbf{I} + \sin(\omega\Delta t)\mathbf{J}] \tag{9}$$

with

$$\mathbf{I} \equiv \begin{pmatrix} 1 & 0 \\ 0 & 1 \end{pmatrix} \quad \text{and} \quad \mathbf{J} \equiv \begin{pmatrix} \frac{1}{2\omega\tau} & \frac{1}{\omega} \\ \frac{-\omega_0^2}{\omega} & \frac{-1}{2\omega\tau} \end{pmatrix}. \tag{10}$$

That the matrix exponential can be written this way can be proven in several ways. We used the algebra of Pauli matrices. Alternatively, one may observe that the cosine and sine terms on the right-hand side are the even and odd parts of the left-hand side. The latter are straightforwardly, if tediously, computed from the Taylor series for the exponential. Inserting Eq. (9) in Eq. (8) we see that

$$\Delta x_j = \frac{\sqrt{2D}}{\omega\tau}\int_{t_j}^{t_{j+1}} dt\, e^{-\frac{t_{j+1}-t}{2\tau}}\,\sin(\omega(t_{j+1}-t))\,\eta(t), \tag{11}$$

$$\Delta v_j = -\frac{\sqrt{2D}}{2\omega\tau^2}\int_{t_j}^{t_{j+1}} dt\, e^{-\frac{t_{j+1}-t}{2\tau}}\,\sin(\omega(t_{j+1}-t))\,\eta(t) + \frac{\sqrt{2D}}{\tau}\int_{t_j}^{t_{j+1}} dt\, e^{-\frac{t_{j+1}-t}{2\tau}}\,\cos(\omega(t_{j+1}-t))\,\eta(t) \tag{12}$$

are two correlated random numbers from zero-mean Gaussian distributions. They can be written as a linear combination of two independent Gaussian variables: The four parameters that determine this linear combination can be chosen at will, as long as the combination has the same variance-covariance as the two original correlated variables. This is a direct consequence of the Gaussian distribution being completely determined by its mean and variance-covariance. Thus, we can write

$$\Delta x_j = \sigma_{xx}\,\xi_j, \tag{13}$$

$$\Delta v_j = \sigma_{xv}^2/\sigma_{xx}\,\xi_j + \sqrt{\sigma_{vv}^2 - \sigma_{xv}^4/\sigma_{xx}^2}\,\zeta_j, \tag{14}$$

where the σs are elements of the variance-covariance matrix (see below), and ξ and ζ are independent random numbers with Gaussian distribution, unit variance, and zero mean. This particular choice of linear combination mirrors the structure of Eqs. (11) and (12). Using Eqs. (3), (11), and (12) we calculate that the elements of the variance-covariance matrix are, for $\omega \neq 0$,

$$\sigma_{xx}^2 \equiv \langle(\Delta x_j)^2\rangle = \frac{D}{4\omega^2\omega_0^2\tau^3}\big(4\omega^2\tau^2 + e^{-\frac{\Delta t}{\tau}}[\cos(2\omega\Delta t) - 2\omega\tau\sin(2\omega\Delta t) - 4\omega_0^2\tau^2]\big), \tag{15}$$

$$\sigma_{vv}^2 \equiv \langle(\Delta v_j)^2\rangle = \frac{D}{4\omega^2\tau^3}\big(4\omega^2\tau^2 + e^{-\frac{\Delta t}{\tau}}[\cos(2\omega\Delta t) + 2\omega\tau\sin(2\omega\Delta t) - 4\omega_0^2\tau^2]\big), \tag{16}$$

$$\sigma_{xv}^2 \equiv \langle\Delta x_j\Delta v_j\rangle = \frac{D}{\omega^2\tau^2}e^{-\frac{\Delta t}{\tau}}\sin^2(\omega\Delta t). \tag{17}$$

At critical damping ($\omega = 0$) this variance-covariance simplifies to

$$\sigma_{xx}^2 \equiv \langle(\Delta x_j)^2\rangle = 4D\tau\big(1 - e^{-\frac{\Delta t}{\tau}}[1 + \Delta t/\tau + \tfrac{1}{2}(\Delta t/\tau)^2]\big), \tag{18}$$

$$\sigma_{vv}^2 \equiv \langle(\Delta v_j)^2\rangle = \frac{D}{\tau}\left(1 - e^{-\frac{\Delta t}{\tau}}\left[1 - \Delta t/\tau + \frac{1}{2}(\Delta t/\tau)^2\right]\right), \tag{19}$$

$$\sigma_{xv}^2 \equiv \langle\Delta x_j\Delta v_j\rangle = De^{-\frac{\Delta t}{\tau}}(\Delta t/\tau)^2. \tag{20}$$

Figure 1 shows the simulated positions in the underdamped, critically damped, and overdamped regimes. Note

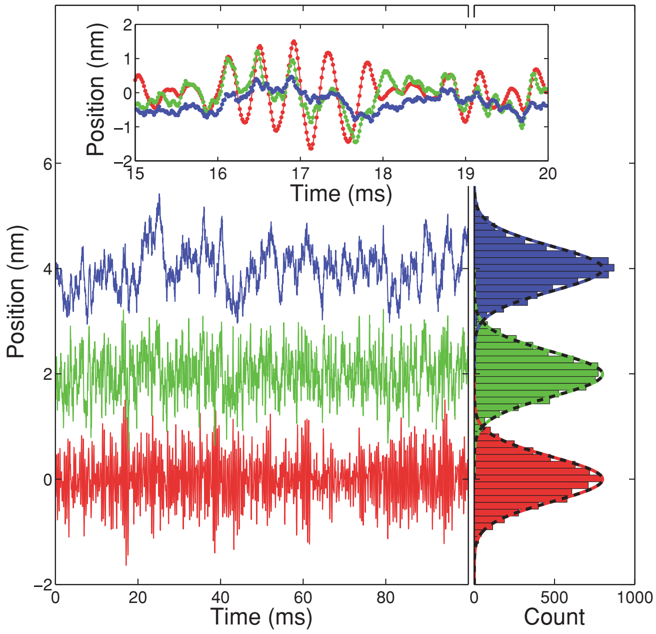

FIG. 1. (Color online) Positions of harmonically trapped massive particles in a thermal bath. Three different regimes are studied by varying the drag coefficient above and below the critical value, where $\omega = 0$, by an order of magnitude: Underdamped [red (gray), $\gamma = \gamma^{\text{crit}}/10$], critically damped [green (light gray), $\gamma = \gamma^{\text{crit}}$, offset by 2 nm], and overdamped [blue (dark gray), $\gamma = 10\,\gamma^{\text{crit}}$, offset by 4 nm]. Simulation parameters in Eq. (7): $m = 1$ ng, $\kappa = 225$ mg/s^2, $T = 275$ K, $f_{\text{sample}} = 65{,}536$ Hz, $(x(0), v(0)) = (0,0)$, and the same (ξ_j, η_j) are used for the three simulations. The values for the underdamped case are alike to those for an AFM cantilever in water, whereas the critical and overdamped cases correspond to the same cantilever in a more viscous environment or with a smaller spring constant. The inset shows a magnified portion of the trace, revealing the oscillating, critical, and random nature of the motion, respectively. On the right, histograms show the distribution of the position data with $k_B T/\kappa$-variance Gaussians overlaid.

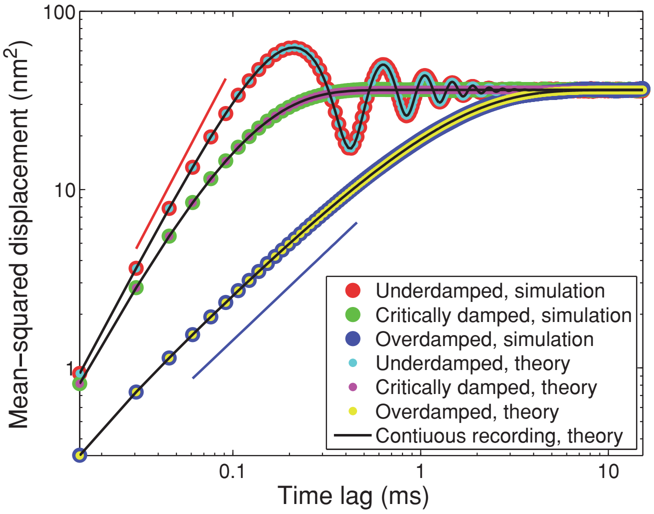

FIG. 2. (Color online) Mean-squared displacements for harmonically trapped massive particles. Same simulation conditions as in Fig. 1, except $t_{\text{msr}} = 8$ s. The result of the stochastic simulations are shown in red (gray), green (light gray), and blue (dark gray). Complementary colors [cyan (light gray), magenta (gray), and yellow (lighter gray); see legend] show the MSD, Eq. (21), evaluated at discrete time points with the same parameter values as in the simulation. Thin black lines show the MSD, Eq. (21), for continuous time. Red (gray, upper) and blue (dark gray, lower) lines show slopes of 2 and 1, respectively. Notice how the MSDs all plateau at the same level for time lags larger than 3 s. Only for shorter time lags do the three regimes differ.

that all three regimes have the same mean (zero) and variance ($k_B T/\kappa$). Only at short times, as shown in the inset, does the difference between the three regimens reveal itself: The position coordinate of the underdamped system oscillates, while the position coordinate of the overdamped system does not show discernible persistence of motion. The position coordinate of the critically damped system looks at times like it oscillates, but actually only displays positively correlated random motion, as revealed by the velocity autocorrelation function given below and shown in Fig. 3(b).

III. MEAN-SQUARED DISPLACEMENT

When a time series of positions is examined, the first measure applied is frequently the mean-squared displacement (MSD). This has to do with its ease of computation, the existence of exact analytical results for the expectation value, and comparative robustness of the measure to experimental measurement errors. Also, there are no discretization effects to worry about—the MSD for finite sampling frequency is simply the MSD for continuous recording, evaluated at discrete time points. More importantly, unlike the covariance and the power spectra discussed below, the MSD is well defined even if the process is not bounded. In the present example, both the position and velocity processes are bounded, and we therefore have a simple relation between the MSD and the autocovariance:

$$\text{MSD}(t) \equiv \langle [x(t) - x(0)]^2 \rangle = 2\langle x^2 \rangle - 2\langle x(t)x(0) \rangle, \quad (21)$$

where $\langle x^2 \rangle = k_B T/\kappa$; i.e., the MSD is a constant minus twice the autocovariance of the position process (see Sec. IV). This is illustrated in Fig. 2, where we show the MSD for the three time series plotted in Fig. 1.

IV. COVARIANCE

The stationary-state solution given in Eq. (6) oscillates in resonating response to the thermal noise that drives it, which is seen by its oscillating autocovariance functions, but its oscillations are randomly phase shifted by the same noise that drives oscillations, which causes the exponential decay in autocovariance functions, see below. The result is that equal-time ensemble averages like $\langle x(t)^2 \rangle$ are constant in time. This is easily proven for quadratic expressions, either directly from the solution given in Eq. (6) or by differentiation with respect to time using Itō's lemma:

$$\frac{d}{dt}\begin{pmatrix}\langle x^2\rangle\\ \langle xv\rangle\\ \langle v^2\rangle\end{pmatrix} = \begin{pmatrix}0 & 2 & 0\\ -\omega_0^2 & \frac{-1}{\tau} & 1\\ 0 & -2\omega_0^2 & \frac{-2}{\tau}\end{pmatrix}\begin{pmatrix}\langle x^2\rangle\\ \langle xv\rangle\\ \langle v^2\rangle\end{pmatrix} + \begin{pmatrix}0\\ 0\\ \frac{2D}{\tau^2}\end{pmatrix}. \qquad (22)$$

As is seen by inspection, this equation has the time-independent solution

$$\begin{pmatrix}\langle x^2\rangle\\ \langle xv\rangle\\ \langle v^2\rangle\end{pmatrix} = \begin{pmatrix}\frac{k_BT}{\kappa}\\ 0\\ \frac{k_BT}{m}\end{pmatrix}, \qquad (23)$$

in accord with the equipartition theorem. This solution is the unique attractor for the system's dynamics: Left to itself, any discrepancy from this time-independent solution will decrease to zero exponentially fast in time—possibly while oscillating harmonically with cyclic frequency 2ω—as is seen from the fact that the 3×3 matrix in Eq. (23) has eigenvalues $-1/\tau$ and $-1/\tau \pm i2\omega$, and determinant $-4\omega_0^2/\tau$.

Similar reasoning [or simply multiplying Eq. (7) by (x_j, v_j), then taking the expectation value and applying the equipartition theorem] gives the covariances

$$\begin{pmatrix}\langle x(t)x(0)\rangle & \langle x(t)v(0)\rangle\\ \langle v(t)x(0)\rangle & \langle v(t)v(0)\rangle\end{pmatrix}. = \frac{D}{\tau}e^{-\frac{t}{2\tau}}\begin{pmatrix}\frac{\cos\omega t+\frac{\sin\omega t}{2\omega\tau}}{\omega_0^2} & \frac{\sin\omega t}{\omega}\\ \frac{-\sin\omega t}{\omega} & \cos\omega t - \frac{\sin\omega t}{2\omega\tau}\end{pmatrix}. \qquad (24)$$

For ω real (underdamped system), these covariances oscillate, we see, with amplitudes that decrease exponentially in time with characteristic time 2τ. For ω imaginary (overdamped system), we rewrite Eq. (24) as

$$\begin{pmatrix}\langle x(t)x(0)\rangle & \langle x(t)v(0)\rangle\\ \langle v(t)x(0)\rangle & \langle v(t)v(0)\rangle\end{pmatrix} = \frac{D}{2|\omega|\tau}\left\{\begin{pmatrix}\frac{1}{\omega_0^2\tau_+} & 1\\ -1 & \frac{-1}{\tau_-}\end{pmatrix}e^{-t/\tau_-} + \begin{pmatrix}\frac{-1}{\omega_0^2\tau_-} & -1\\ 1 & \frac{1}{\tau_+}\end{pmatrix}e^{-t/\tau_+}\right\}, \qquad (25)$$

from which we see that the system decreases as a double exponential with characteristic times $\tau_\pm = 2\tau/(1 \pm 2\tau|\omega|)$. At critical damping ($\omega = 0$), the expressions for the covariances simplify to

$$\begin{pmatrix}\langle x(t)x(0)\rangle & \langle x(t)v(0)\rangle\\ \langle v(t)x(0)\rangle & \langle v(t)v(0)\rangle\end{pmatrix} = \frac{D}{\tau}e^{-\frac{t}{2\tau}}\begin{pmatrix}\frac{1+t/(2\tau)}{\omega_0^2} & t\\ -t & 1-t/(2\tau)\end{pmatrix}. \qquad (26)$$

Figure 3 illustrates these dynamics for the normalized covariances, a.k.a. the correlation functions.

As is the case for the MSD, there are no discretization effects to worry about—the covariance for finite sampling frequency is simply the covariance for continuous recording,

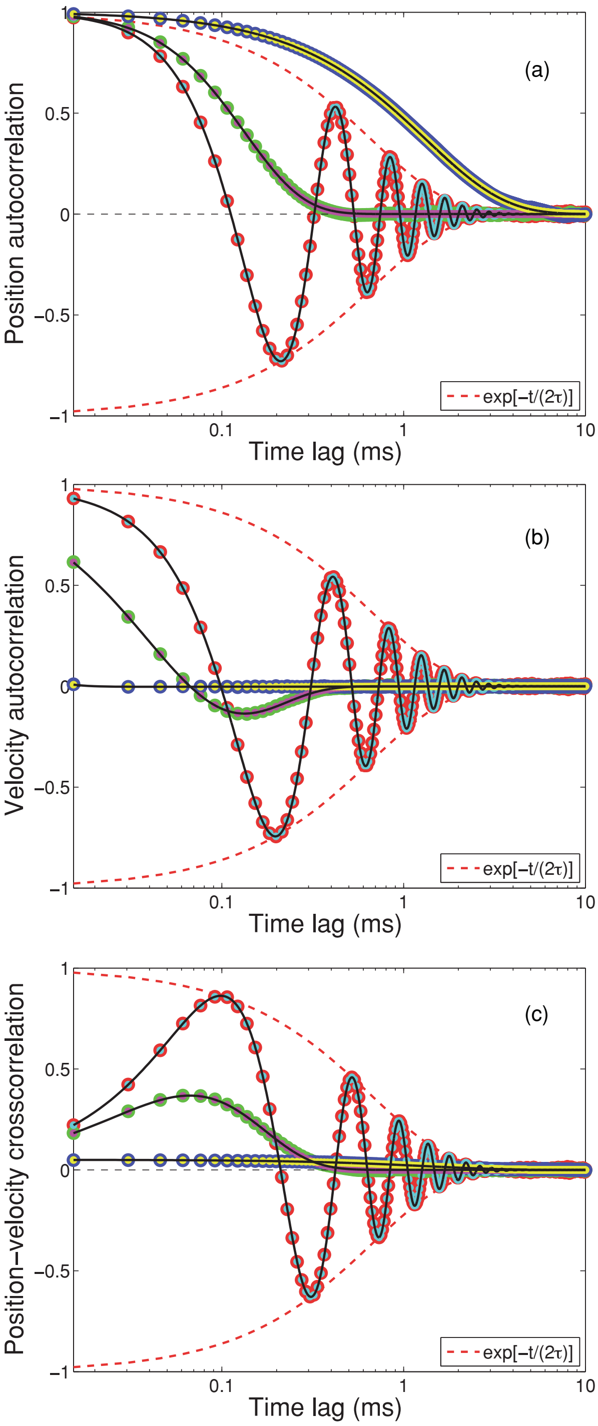

FIG. 3. (Color online) Correlation functions, Eq. (24), for massive particles in a harmonic potential, driven by thermal noise. Color coding and simulation settings are the same as in Fig. 2: Red (gray), green (light gray), and blue (dark gray) show the result of a stochastic simulation; complementary colors show the covariance (not a fit), Eq. (24), normalized and evaluated at discrete time points; thin black lines show the covariance for continuous time (not a fit); and dashed red (gray) lines show the enveloping exponential $\exp(-t/(2\tau))$. (a) Position autocorrelations, $\langle x(t)x(0)\rangle/\langle x^2\rangle$. (b) Velocity autocorrelations, $\langle v(t)v(0)\rangle/\langle v^2\rangle$. (c) Position-velocity cross correlations, $\langle x(t)v(0)\rangle/\sqrt{\langle x^2\rangle\langle v^2\rangle}$. The velocity-position cross correlation, $\langle v(t)x(0)\rangle/\sqrt{\langle x^2\rangle\langle v^2\rangle}$ (not shown), has the opposite sign but is otherwise identical.

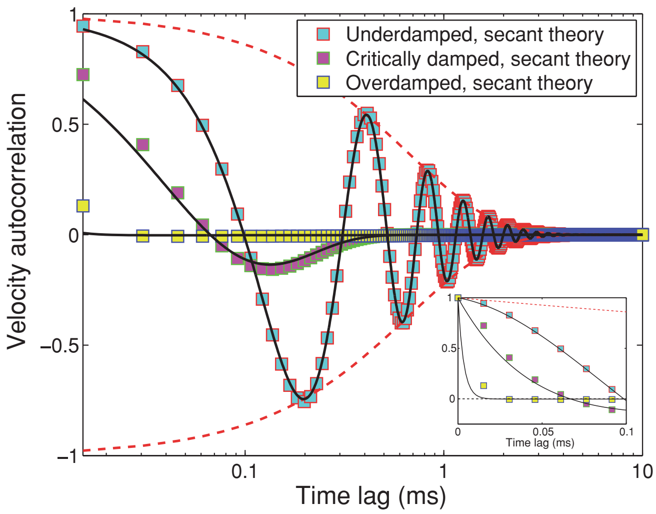

FIG. 4. (Color online) Secant-velocity autocorrelation functions for massive particles in a harmonic potential, driven by thermal noise. Thin black lines, red (gray) dashed lines, and simulation settings are the same as in Fig. 3(b). Additional symbols: Cyan (light gray) squares with red (gray) borders, magenta (dark gray) squares with green (light gray) borders, and yellow (lighter gray) squares with blue (dark gray) borders show the autocorrelations for $w_j = (x_j - x_{j-1})/\Delta t$ calculated using $\langle x(t)x(0)\rangle$ from Eq. (24). Inset shows the first 0.1 ms on a linear time scale, revealing the very fast decay of the overdamped oscillator and how the secant-velocity autocorrelations overestimate the instantaneous-velocity autocorrelation decay times. As expected, the secant velocity does a better job of estimating the instantaneous velocity for the less damped system because of its smoother particle trajectory.

evaluated at discrete time points. However, the given velocity correlations, and thus also the position-velocity correlations, are only correct for the actual, instantaneous velocities: If the instantaneous velocity is not directly measured, but instead estimated from measured positions as a “secant velocity” [see Eq. (60) and Sec. VII A 1], then the corresponding secant-velocity correlation function should be calculated from the position covariance function given in Eq. (24). Figure 4 shows how such secant-velocity correlations deviate from the instantaneous-velocity correlations, mainly for short time lags.

V. POWER SPECTRA

The power spectral density (PSD) of a variable $x(t)$ or $v(t)$ is defined as the expectation value of the squared modulus of its Fourier transform, with a normalization that differs between authors. We choose one in which the power spectral density remains constant for increasing measurement time t_{msr}:

$$P^{(x)}(f_k) \equiv \langle|\tilde{x}_k|^2\rangle/t_{\mathrm{msr}} = \frac{D/(2\pi^2)}{(2\pi\tau)^2\left(f_k^2 - f_0^2\right)^2 + f_k^2} \tag{27}$$

and

$$\begin{aligned} P^{(v)}(f_k) &\equiv \langle|\tilde{v}_k|^2\rangle/t_{\mathrm{msr}} = (2\pi f_k)^2 P^{(x)}(f_k) \\ &= \frac{2D}{(2\pi\tau)^2\left(f_k - f_0^2/f_k\right)^2 + 1}, \end{aligned} \tag{28}$$

where $2\pi f_0 = \omega_0$ is the resonance frequency of the system. Here, we use $\tilde{v}_k = i2\pi\tilde{x}_k$, which is an approximation that ignores contributions from the finite measurement time.

The finite-time Fourier transform (FTFT) used above is defined as

$$\tilde{x}_k = \int_0^{t_{\mathrm{msr}}} dt\, e^{i2\pi f_k t}\, x(t), \quad f_k \equiv k/t_{\mathrm{msr}}, \quad k = \text{integer}. \tag{29}$$

In a similar manner we can calculate the finite-sampling-frequency PSDs by discrete Fourier transformation (DFT) of Eq. (7):

$$e^{-i\pi f_k/f_{\mathrm{Nyq}}}\begin{pmatrix}\hat{x}_k\\ \hat{v}_k\end{pmatrix} = e^{-\mathbf{M}\Delta t}\begin{pmatrix}\hat{x}_k\\ \hat{v}_k\end{pmatrix} + \begin{pmatrix}\Delta\hat{x}_k\\ \Delta\hat{v}_k\end{pmatrix}, \tag{30}$$

where

$$\hat{z}_k = \Delta t \sum_{j=1}^{N} e^{i2\pi jk/N} z_j = \frac{2}{f_{\mathrm{Nyq}}} \sum_{j=1}^{N} e^{i\pi j f_k/f_{\mathrm{Nyq}}} z_j, \tag{31}$$

for $z = x, v, \Delta x, \Delta v$; $x_{N+1} = x_1$ and $v_{N+1} = v_1$;

$$f_k = k\Delta f = k/t_{\mathrm{msr}}, \tag{32}$$

$$k = 0,1,2,\ldots,N-1, \tag{33}$$

$$t_{\mathrm{msr}} = N\,\Delta t = N/f_{\mathrm{sample}}, \tag{34}$$

$$f_{\mathrm{Nyq}} = \frac{N}{2}\Delta f = \frac{f_{\mathrm{sample}}}{2}, \tag{35}$$

and

$$\langle\Delta\hat{x}_k^*\Delta\hat{x}_{k'}\rangle = \sigma_{xx}^2\,\langle\hat{\xi}_k^*\hat{\xi}_{k'}\rangle = \sigma_{xx}^2\,\Delta t\, t_{\mathrm{msr}}\,\delta_{k,k'}, \tag{36}$$

$$\langle\Delta\hat{v}_k^*\Delta\hat{v}_{k'}\rangle = \sigma_{vv}^2\,\Delta t\, t_{\mathrm{msr}}\,\delta_{k,k'}, \tag{37}$$

$$\langle\Delta\hat{x}_k^*\Delta\hat{v}_{k'}\rangle = \sigma_{xv}^2\,\Delta t\, t_{\mathrm{msr}}\,\delta_{k,k'}. \tag{38}$$

After isolating $(\hat{x}_k, \hat{v}_k)$ in Eq. (30), we find

$$\begin{pmatrix}\langle|\hat{x}_k|^2\rangle & \langle\hat{x}_k\hat{v}_k^*\rangle\\ \langle\hat{x}_k^*\hat{v}_k\rangle & \langle|\hat{v}_k|^2\rangle\end{pmatrix} = \mathbf{A}_k^{-1}\begin{pmatrix}\sigma_{xx}^2 & \sigma_{xv}^2\\ \sigma_{xv}^2 & \sigma_{vv}^2\end{pmatrix}(\mathbf{A}_k^\dagger)^{-1}\, t_{\mathrm{msr}}\Delta t, \tag{39}$$

where the 2×2 matrix and its inverse are

$$\mathbf{A}_k = \alpha_k\mathbf{I} + \beta\mathbf{J}\,, \quad \mathbf{A}_k^{-1} = \frac{\alpha_k\mathbf{I} - \beta\mathbf{J}}{\alpha_k^2 + \beta^2}, \tag{40}$$

with

$$\alpha_k = e^{-i\pi f_k/f_{\mathrm{Nyq}}} - e^{-\frac{\Delta t}{2\tau}}\cos(\omega\Delta t), \tag{41}$$

$$\beta = -e^{-\frac{\Delta t}{2\tau}}\sin(\omega\Delta t), \tag{42}$$

complex scalars (β/ω is real), Hermitian conjugation denoted by †, and complex conjugation by $*$.

For the discrete positional power spectrum we thus get (see also Appendix A of [1])

$$\begin{aligned} P_k^{(x)} &\equiv \langle|\hat{x}_k|^2\rangle/t_{\mathrm{msr}} \\ &= \frac{\left|\alpha_k - \frac{\beta}{2\omega\tau}\right|^2\sigma_{xx}^2 - 2\frac{\beta}{\omega}\,\mathrm{Re}\left\{\alpha_k - \frac{\beta}{2\omega\tau}\right\}\sigma_{xv}^2 + \frac{\beta^2}{\omega^2}\sigma_{vv}^2}{\left|\alpha_k^2 + \beta^2\right|^2\, f_{\mathrm{sample}}} \end{aligned} \tag{43}$$

whereas the discrete velocity power spectrum is

$$P_k^{(v)} \equiv \langle |\hat{v}_k|^2 \rangle / t_{\mathrm{msr}}$$
$$= \frac{\left|\alpha_k + \frac{\beta}{2\omega\tau}\right|^2 \sigma_{vv}^2 + 2\omega_0^2 \frac{\beta}{\omega} \,\mathrm{Re}\left\{\alpha_k + \frac{\beta}{2\omega\tau}\right\}\sigma_{xv}^2 + \omega_0^4 \frac{\beta^2}{\omega^2}\sigma_{xx}^2}{\left|\alpha_k^2 + \beta^2\right|^2 f_{\mathrm{sample}}}. \tag{44}$$

In the case of critical damping ($\omega = 0$) we simply insert $\beta/\omega = -e^{-\frac{\Delta t}{2\tau}} \Delta t$ in Eqs. (43) and (44), and use Eqs. (18), (19), and (20) for the variance-covariances.

Figure 5 shows the power spectra that result from numerical simulations of AFM cantilever positions and velocities using Eq. (7) for three different drag coefficients, as well as the corresponding analytical expressions as given in Eqs. (43) and (44).

An alternative route to these discrete PSDs is to take the discrete Fourier transform of the covariance function from the previous section: Both the position and the velocity processes are stationary (the joint probability density function for each is independent of time), so the Wiener-Khinchin theorem applies and the Fourier transform of the correlation function is equal to the PSD. For vanishing spring constant κ, the position process is unbounded (not stationary) and the covariance, as well as the PSD, is consequently ill defined. This limit is treated in Sec. VII A.

Note, the PSD for discretely measured (instantaneous) velocities, Eq. (44), should not be confused with the discrete PSD for secant velocities, Eq. (61). The latter is the correct expression to use in experiments where the velocities are estimated from the measured positions.

VI. VANISHING Δt: THE LIMIT OF CONTINUOUS RECORDING

As $\Delta t \to 0$ we find to first order in Δt that the covariances in Eqs. (15)–(20) reduce to $\sigma_{xx}^2 = 0$, $\sigma_{vv}^2 = 2D\Delta t/\tau^2$, and $\sigma_{xv}^2 = 0$. That is, $\Delta x_j = 0$ and $\Delta v_j = \sigma_{vv}\zeta_j = \sqrt{2D\Delta t}/\tau\, \zeta_j$. In other words, the velocity process is seen to be driving the position process.

In this limit the positional PSD takes on the familiar form given in Eq. (27), and the velocity PSD is given in Eq. (28). Comparing the continuous-recording PSDs, Eqs. (27) and (28), with their discrete sampling analogues, Eqs. (43) and (44), we see in Fig. 5(a) that they differ substantially at high frequencies, and in Fig. 5(b) that they differ everywhere but near f_0 in the underdamped case. Thus, one should not attempt to fit a theoretical PSD derived for "continuously recorded" trajectories to an experimental PSD, which necessarily is obtained with time-lapse recording. More specifically, one should only attempt to fit it to the low-frequency part of the experimental spectrum for positions, or account for "aliasing" before fitting, as described, e.g., in Appendix H of [9], which turns Eqs. (27) and (28) into Eqs. (43) and (44), respectively.

The position covariance and the MSD do not suffer from this dichotomy. Neither of them changes its shape or form when switching between discrete and continuous time: The discrete versions are equal to the continuous versions, evaluated at discrete times:

$$\langle x_j x_{j+\ell} \rangle = \langle x(t_j) x(t_{j+\ell}) \rangle = \langle x(0) x(t_\ell) \rangle \tag{45}$$

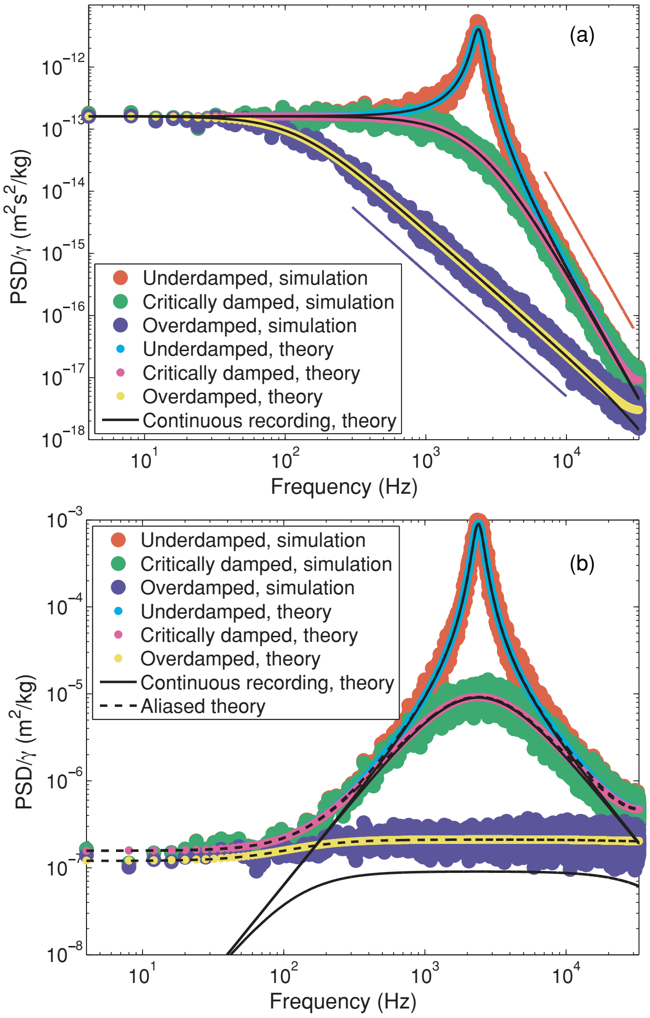

FIG. 5. (Color online) Power spectra for positions and velocities of harmonically trapped massive particles in thermal bath, normalized by γ. The color scheme is the same as in Figs. 2 and 3: Synthetic data are shown in red (gray), green (light gray), and blue (dark gray); the aliased theory, Eqs. (43) and (44), is shown in complementary colors; and the nonaliased theory, Eqs. (27) and (28), as thin black lines. Simulation parameters are as in Fig. 1 (giving $\omega_0 = 15$ kHz) with $n_{\mathrm{win}} = 32$ Hann windows applied to the $t_{\mathrm{msr}} = 8$ s long time series. (a) Power spectra for positions. Thin blue (dark gray, lower) and red (gray, upper) lines illustrate f^{-2} and f^{-4} behaviors, respectively. Notice the disagreement between the nonaliased (continuous recording) theory and data at high frequencies. (b) Power spectra for velocities. Dashed black lines show aliased versions of Eq. (28); i.e., $P^{(v,\mathrm{aliased})}(f) = \sum_{n=-\infty}^{\infty} P^{(v)}(f + n f_{\mathrm{sample}})$ [9], here truncated to 201 terms. The nonaliased theory severely underestimates the power at high and low frequencies, and completely misses the data in the overdamped case.

and

$$\langle (x_j - x_{j+\ell})^2 \rangle = \langle [x(t_j) - x(t_{j+\ell})]^2 \rangle = \langle [x(0) - x(t_\ell)]^2 \rangle, \tag{46}$$

where, in the last step, we used that the process is stationary and the measures therefore invariant to time translations. That is, these measures are unaffected by the unavoidable discreteness of real-world data.

The velocity's covariance is also unaffected by time-lapse recording, if we can measure the instantaneous velocity, i.e., the velocity vector that is tangential to the trajectory of the position. If we cannot and time-lapse-record only positions, we have a different situation, which is treated below.

VII. VARIOUS PHYSICAL LIMITS: A REFERENCE SET OF FORMULAS

Three physical limiting cases are of particular interest: (i) Vanishing spring constant, $\kappa = 0$, which is the Ornstein-Uhlenbeck theory for Brownian motion for a free particle with inertia; (ii) vanishing mass, $m = 0$, which is Einstein's theory for Brownian motion of a particle trapped by a Hookean force, and a popular minimalist model of the Brownian motion of a microsphere in an optical trap; and (iii) vanishing mass and spring constant, which is Einstein's theory for Brownian motion of a free particle.

A. Vanishing spring constant: The Ornstein-Uhlenbeck process

When there is no Hookean restoring force $\kappa = 0$, Eq. (1) describes the free diffusion of a massive particle according to Ornstein and Uhlenbeck [4]:

$$m\dot{v}(t) + \gamma v(t) = F_{\text{therm}}(t). \tag{47}$$

This velocity process is known as the Ornstein-Uhlenbeck (OU) process [4]. When modeling other dynamical systems, such as migrating cells, m does not refer to the physical mass of the cell but rather its inertia to velocity changes, or persistence of motion; likewise γ is not the friction between the cell and substrate but describes the rate of memory loss for the velocity process. The structure of Eqs. (7), (9), (10), (13), and (14) remains the same; the only change is $\omega_0 = 0$ in Eq. (10), hence $\omega = i/(2\tau)$, and the covariances, Eqs. (15), (16), and (17), consequently reduce to

$$\sigma_{xx}^2 = D\tau[2\Delta t/\tau - 4(1-a) + (1-a^2)], \tag{48}$$

$$\sigma_{vv}^2 = D(1-a^2)/\tau, \tag{49}$$

$$\sigma_{xv}^2 = D\,(1-a)^2\,, \tag{50}$$

where

$$a = e^{-\Delta t/\tau}, \quad \tau = m/\gamma. \tag{51}$$

For the velocity and position processes we thus find

$$v_{j+1} = a v_j + \Delta v_j, \tag{52}$$

$$x_{j+1} = x_j + \tau(1-a)v_j + \Delta x_j. \tag{53}$$

That is, the velocity process has reduced to a stable autoregressive model of order 1, AR(1). Its time integral, the position process, is unbounded—the particle is diffusing freely and without limits. Exact numerical update formulas for v_j and x_j have previously been given in [3]; here we rederived them for consistency of notation.

The discrete-time positional PSD, $P_k^{(x)}$, is obtainable from Eq. (43) with $\omega_0 = 0$ and the σs given in Eqs. (48), (49), and (50); the expression does not simplify significantly compared to Eq. (43). The discrete-time velocity PSD, $P_k^{(v)}$, is much simpler and can be derived directly from the discrete-time velocity process, Eq. (52), or by taking the $\kappa = 0$ limit of Eq. (44). From these discrete-time PSDs the continuous-recording expressions, $P^{(x)}(f_k)$ and $P^{(v)}(f_k)$, can be obtained by expanding to leading order in $\Delta t/\tau$ and $k/N = f_k/f_{\text{sample}}$; or they can be derived directly from the continuous-time equation of motion Eq. (47) by Fourier transformation and, for the positional PSD, remembering that $\dot{x} = v$. The continuous-recording positional PSD and the two velocity PSDs then read

$$P^{(x)}(f_k) = \frac{D/(2\pi^2)}{(2\pi\tau)^2 f_k^4 + f_k^2}, \tag{54}$$

$$P_k^{(v)} = \frac{\sigma_{vv}^2\ \Delta t}{1 + a^2 - 2a\cos(2\pi k/N)}, \tag{55}$$

$$P^{(v)}(f_k) = \frac{2D}{1 + (2\pi f_k \tau)^2}. \tag{56}$$

Note that the positional PSD diverges in $f_k = 0$ due to the process being unbounded. This implies that we cannot use the Wiener-Khinchin theorem to obtain the covariance by Fourier transforming the PSDs, and vice versa. The velocity process is bounded, however, and the velocity correlation functions are straightforward to calculate, so we simply list the results for the discrete and the continuous cases:

$$\langle v_i v_j \rangle = \frac{D}{\tau}\ e^{-|i-j|\Delta t/\tau}, \tag{57}$$

$$\langle v(t)v(t')\rangle = \frac{D}{\tau}\ e^{-|t-t'|/\tau}. \tag{58}$$

As already mentioned, the time integral of the OU process is one of the instances where the mean-squared displacement provides a useful measure for the position process, while the positional covariance function is ill defined. The mean-squared displacement of the time integral of the OU process is

$$\langle [x(t) - x(0)]^2 \rangle = 2D\tau(t/\tau + e^{-t/\tau} - 1). \tag{59}$$

For $t \ll \tau$ this MSD increases as t^2 (ballistically) and for $t \gg \tau$ as t (diffusively), with an exponential crossover between the two regimes with characteristic time τ.

1. *Secant velocities*

In experiments, the velocity is typically not measured directly, but approximated from the measured positions as a "secant velocity":

$$w_j = (x_j - x_{j-1})/\Delta t \tag{60}$$

with discrete power spectral density

$$P_k^{(w)} \equiv \langle |\hat{w}_k|^2 \rangle / t_{\text{msr}} = \frac{2[1 - \cos(\pi f_k/f_{\text{Nyq}})]}{(\Delta t)^2}\ P_k^{(x)}. \tag{61}$$

This is a general result that follows from the definition of w_j and is independent of the dynamic model.

For the OU process, we can relate this PSD to the PSD for the continuous velocity that it approximates, if we rewrite it as

$$\begin{aligned} P_k^{(w)} = {} & P_k^{(v)}(\tau/\Delta t)^2(1-a)^2 + \sigma_{xx}^2/\Delta t \\ & + \tau(1-a)(\langle \hat{v}_k^*\ \Delta\hat{x}_k \rangle + \text{c.c.}). \end{aligned} \tag{62}$$

Here the first term is proportional to $P_k^{(v)}$, the second term is a constant, and the last term is frequency dependent with c.c., the complex conjugate of the other term in the bracket. However, it is not easy to see from this expression how much

$P_k^{(w)}$ deviates from $P_k^{(v)}$. We can get a good idea about the shape of the PSD from the autocorrelation function,

$$\langle w_j^2\rangle = 2\langle v_j^2\rangle\left(\frac{\tau}{\Delta t}\right)^2(\Delta t/\tau - 1 + a) \tag{63}$$

$$\approx \langle v_j^2\rangle\left(1-\frac{1}{3}\Delta t/\tau\right), \tag{64}$$

and for $\ell > 0$,

$$\langle w_j w_{j+\ell}\rangle = 2\langle v_j v_{j+\ell}\rangle\left(\frac{\tau}{\Delta t}\right)^2[\cosh(\Delta t/\tau) - 1] \tag{65}$$

$$\approx \langle v_j v_{j+\ell}\rangle\left(1+\frac{1}{12}(\Delta t/\tau)^2\right), \tag{66}$$

where we used Eqs. (13), (14), (50), (53), and (57) to derive Eqs. (63) and (65)—the latter two expressions are proportional to the velocity autocorrelations they approximate; they only differ by multiplicative factors that are independent of the time lag for $\ell > 0$. To first order in $\Delta t/\tau$ we thus have, for $\ell \geqslant 0$,

$$\langle w_j w_{j+\ell}\rangle = \langle v_j v_{j+\ell}\rangle\left(1-\frac{1}{3}\frac{\Delta t}{\tau}\delta_{0,\ell}\right). \tag{67}$$

We now apply the Wiener-Khinchin theorem to get the PSD as the Fourier transform of this approximated auto-correlation function and find

$$P_k^{(w)} \approx P_k^{(v)} - \frac{1}{3}\left(\frac{\Delta t}{\tau}\right)^2 D. \tag{68}$$

This approximation to the secant-velocity PSD, as well as the exact expression Eq. (61), are both shown in Fig. 6, together with numerical simulation results and the PSD of the continuous velocity Eq. (55). Notice that even with $\Delta t/\tau = 0.27 < 1$ ($\Delta t = 1/f_{\text{sample}}$ and $\tau = m/\gamma$), the relative difference between $P_k^{(v)}$ and $P_k^{(w)}$ is substantial for higher frequencies. Thus, proper care should be taken if empirical testing of a model includes the fitting of a theoretical velocity PSD to an experimental secant-velocity PSD, even when aliasing is properly accounted for. But, we now also know how to do this correctly: Either add $1/3(\Delta t/\tau)^2 D$ to the experimental secant-velocity PSD before fitting with $P_k^{(v)}$, or fit directly using the full theoretical expression for $P_k^{(w)}$ given in Eq. (61). In cases where this corrective constant is much smaller than the velocity PSD *for all frequencies fitted*, it can obviously be ignored.

We observe that the secant velocity is the time average of the real velocity in the time interval spanned by the secant. Time averaging is low-pass filtering, as is well known, see Chapter 13 in [28], and demonstrated in Fig. 6.

B. Vanishing mass: The optical trap limit

The *position* process in the limit of vanishing mass is mathematically identical to the OU *velocity* process in the limit of vanishing trapping force treated above. Equation (1) reduces to

$$\gamma\dot{x}(t) + \kappa x(t) = F_{\text{therm}}(t) \tag{69}$$

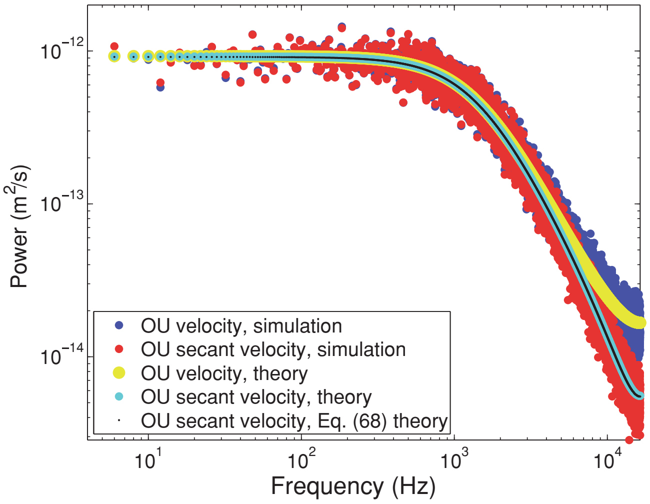

FIG. 6. (Color online) Power spectra of velocities and secant velocities for the OU process. Blue (dark gray): Simulated velocities, Eq. (52). Red (gray): Secant velocities, Eq. (60), calculated from simulated positions, Eq. (53). Yellow (lighter gray): Aliased velocity theory, Eq. (55). Cyan (light gray, lower): Aliased secant-velocity theory, Eq. (61). Black line: Approximated aliased secant-velocity theory, Eq. (68). See legend for details. Simulation settings are given in the caption of Fig. 7. Notice the discrepancy between the true velocity and the estimated (secant) velocity at high frequencies.

with solution

$$x(t) = \frac{1}{\gamma}\int_{-\infty}^{t} dt'\, e^{-2\pi f_c(t-t')}\, F_{\text{therm}}(t'), \tag{70}$$

where the corner frequency $f_c \equiv \kappa/(2\pi\gamma)$ is the frequency where $P^{(x)}(f_k) = P^{(x)}(0)/2$, see below. Recycling the results from Sec. VII A we can directly write down the autocovariance

$$\langle x(t)x(t')\rangle = \langle x^2\rangle\, e^{-2\pi f_c|t-t'|} \tag{71}$$

with $\langle x^2\rangle = k_B T/\kappa$ and the discrete update rules

$$x_{j+1} = c\, x_j + \Delta x_j, \tag{72}$$

$$c = \exp(-\kappa\Delta t/\gamma), \tag{73}$$

$$\Delta x_j = \sqrt{\frac{(1-c^2)D\gamma}{\kappa}}\,\xi_j, \tag{74}$$

where ξ are uncorrelated random numbers of unit variance, zero mean, and Gaussian distribution. Likewise, the position PSDs for discrete sampling and continuous recording are respectively found to be

$$P_k^{(x)} = \frac{D\,(1-c^2)\,\Delta t\gamma/\kappa}{1 + c^2 - 2c\cos(2\pi k/N)}, \tag{75}$$

$$P^{(x)}(f_k) = \frac{D/(2\pi^2)}{f_c^{\,2} + f_k^2}. \tag{76}$$

Finally, the mean-squared displacement is

$$\langle[x(t) - x(0)]^2\rangle = 2D\gamma/\kappa(1 - e^{-t\gamma/\kappa}), \tag{77}$$

which shows an exponential crossover from linear dependence on t to the constant value $2D\gamma/\kappa$ as $t \gg \kappa/\gamma$, see Fig. 2.

C. Vanishing mass and spring constant: Einstein's Brownian motion

When both $m = 0$ and $\kappa = 0$, Eq. (1) reduces to

$$\gamma \dot{x}(t) = F_{\mathrm{therm}}(t) \tag{78}$$

so that

$$x_{j+1} = x_j + \sqrt{2D\,\Delta t}\;\xi_j, \tag{79}$$

where

$$\xi_j \equiv \frac{1}{\sqrt{\Delta t}} \int_{t_j}^{t_{j+1}} dt\;\eta(t), \tag{80}$$

hence

$$\langle \xi_j \rangle = 0,\; \langle \xi_i \xi_j \rangle = \delta_{i,j}, \tag{81}$$

and the velocity and position PSDs for discrete and continuous sampling take on the simple forms:

$$P_k^{(x)} = \frac{D/{f_{\mathrm{sample}}}^2}{2\sin^2(\pi f_k/f_{\mathrm{sample}})}, \tag{82}$$

$$P^{(x)}(f_k) = \frac{D}{2\pi^2 f_k^2}, \tag{83}$$

$$P_k^{(v)} = P^{(v)}(f_k) = 2D. \tag{84}$$

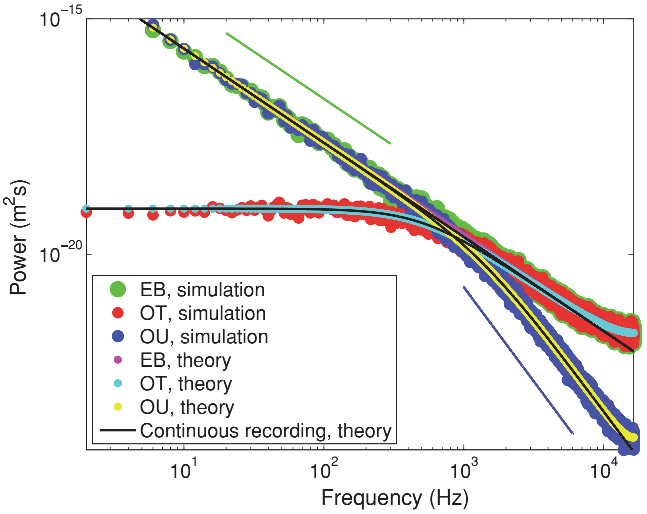

FIG. 7. (Color online) Power spectra of positions. Green points (light gray): Freely diffusing massless particle (Einstein's Brownian motion); red points (gray): trapped massless particle (OT limit, or OU velocity process); and blue (dark gray) points: freely diffusing massive particles (time integral of OU process). Complementary colors show the finite sampling frequency (aliased) theories, whereas the continuous recording (nonaliased) theories are shown as thin black lines. Green (light gray, upper) and blue (dark gray, lower) lines indicate f^{-2} and f^{-4} behavior, respectively. See legend for details. Simulation parameters: $D = 0.46\,\mu\mathrm{m}^2/\mathrm{s}$, $T = 275$ K, $m = 1$ ng, $f_c = 500$ Hz, $f_{\mathrm{sample}} = 32\,768$ Hz, $N = 131\,072$, and $n_{\mathrm{win}} = 32$ Hann windows. The simulation parameters for the OT case are those of a 1 μm diameter polystyrene sphere held in an optical trap in water at room temperature. The parameters for Einstein's Brownian motion are the same, except $\kappa = 0$. For the OU process we increased the density of the sphere roughly 2000 times, which is not a physically realistic scenario but allows us to plot all power spectra with the same axes.

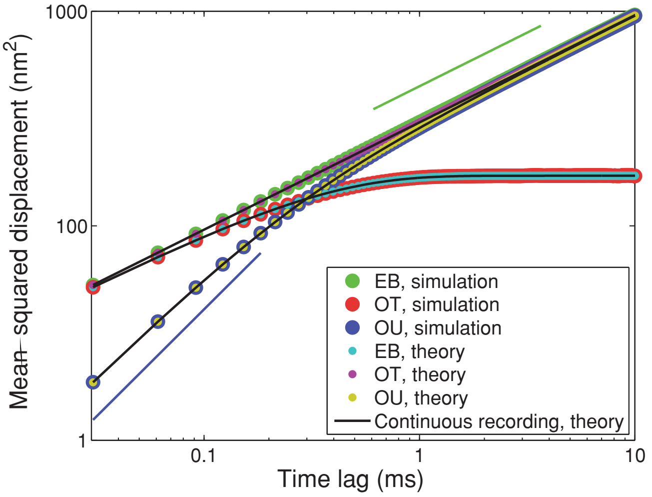

FIG. 8. (Color online) Mean-squared displacement for the Ornstein-Uhlenbeck, optical-trap, and Brownian-motion limits described in Secs. VII A, VII B and VII C. Simulation settings and legends are the same as in Fig. 7, except green (light gray, upper) and blue (dark gray, lower) lines show slopes of 1 and 2, respectively.

As was the case for the time integral of the OU process, the position PSDs are singular in $f_k = 0$ because the process is unbounded. That is, the meaningful measure to study is not the covariance, but rather the mean-squared displacement

$$\langle [x(t) - x(0)]^2 \rangle = 2Dt, \tag{85}$$

which is one of the few well-defined statistics for Einstein's theory of Brownian motion: Because the trajectory of positions is a fractal, attempts at estimating the average speed of Brownian motion from the displacement of position occurring in a given time interval will depend on the duration, Δt, of this interval as $1/\sqrt{\Delta t}$, hence diverge when accuracy is sought improved by reducing Δt. This was not appreciated before Einstein's 1905 paper on the subject.

Figures 7 and 8 show the power spectra and mean-squared displacements, respectively, obtained in numerical simulations of free diffusion and trapped diffusion, as well as the graphs of the corresponding analytical expressions. At short time scales, i.e., at high frequencies in Fig. 7 and for small time lags in Fig. 8, the thermal forces dominate and the Hookean force has not had time to influence the motion through its constant, but weak, confining effect. That is why the Brownian motion (green) and optical trap (red) data collapse in this regime, whereas the Ornstein-Uhlenbeck process (blue) differs from the two due to inertial effects. Conversely, at long time scales, low frequencies in Fig. 7, and large time lags in Fig. 8, inertia plays no role, so the Ornstein-Uhlenbeck process and Einstein's theory of Brownian motion are indistinguishable, whereas the Hookean force has had time to exert its confining effect on the optical trap data.

VIII. SUMMARY AND CONCLUSIONS

We examined the dampened harmonic oscillator and three of its physical limits: The massless case (optical trap), the free case (the Einstein-Ornstein-Uhlenbeck theory of Brownian motion), and the massless free case (Einstein's Brownian motion). By solving the system's dynamical equations for an arbitrary time lapse Δt, exact analytical expressions were derived for the changes in position and velocity during such a time lapse. With these expressions, exact simulations of the dynamics are then possible—with an accuracy that is independent of the duration of the time lapse. In contrast, a numerical simulation, using Euler integration or similar schemes, is exact only to first or second order in Δt [29].

We gave exact analytical expressions for power-spectral forms, mean-squared displacements, and correlation functions that can be fitted (see [1] before undertaking a least-squares fit) to data obtained from time-lapse recording of a system with dynamics similar to the dampened harmonic oscillator or one of its three physical limits described here. The effect of finite sampling rates (aliasing) were also discussed.

The effect on the power spectrum of velocity estimation from position data (secant velocity) was treated for the case of free diffusion of a massive particle. Approximate as well as exact corrective factors and expressions were given. Throughout, we pointed out when power spectral analysis makes sense (bounded process) or does not, which of the statistical measures depend on the sampling frequency, and which may be described by the simpler continuous-time theory.

ACKNOWLEDGMENTS

S.F.N. gratefully acknowledges financial support from the Carlsberg Foundation and the Lundbeck Foundation.

---

[1] S. F. Nørrelykke and H. Flyvbjerg, Rev. Sci. Instrum. **81**, 075103 (2010).
[2] L. Schimansky-Geier and C. Zülicke, Z. Phys. B **79**, 451 (1990).
[3] D. T. Gillespie, Phys. Rev. E **54**, 2084 (1996).
[4] G. Uhlenbeck and L. Ornstein, Phys. Rev. **36**, 823 (1930).
[5] S. Chandrasekhar, Rev. Mod. Phys. **15**, 0001 (1943).
[6] M. C. Wang and G. E. Uhlenbeck, Rev. Mod. Phys. **17**, 323 (1945).
[7] L. S. Ornstein, Proc. R. Acad. Amsterdam **21**, 96 (1919).
[8] H. A. Lorentz, *Lessen over Theoretishe Natuurkunde*, Vol. V (E. J. Brill, Leiden, 1921), Chap. Kinetische Problemen.
[9] K. Berg-Sørensen and H. Flyvbjerg, Rev. Sci. Instrum. **75**, 594 (2004).
[10] K. Berg-Sørensen, E. J. G. Peterman, T. Weber, C. F. Schmidt, and H. Flyvbjerg, Rev. Sci. Instrum. **77**, 063106 (2006).
[11] B. Lukić, S. Jeney, C. Tischer, A. J. Kulik, L. Forró, and E.-L. Florin, Phys. Rev. Lett. **95**, 160601 (2005).
[12] D. Selmeczi, S. F. Tolić-Nørrelykke, E. Schaffer, P. H. Hagedorn, S. Mosler, K. Berg-Sørensen, N. B. Larsen, and H. Flyvbjerg, Acta Phys. Pol. B **38**, 2407 (2007).
[13] D. R. Burnham and D. McGloin, New J. Phys. **11**, 063022 (2009).
[14] D. R. Burnham, P. J. Reece, and D. McGloin, Phys. Rev. E **82**, 051123 (2010).
[15] T. Li, S. Kheifets, D. Medellin, and M. G. Raizen, Science **328**, 1673 (2010).
[16] J. Sader, J. Appl. Phys. **84**, 64 (1998).
[17] M. H. Gail and C. W. Boone, Biophys. J. **10**, 980 (1970).
[18] R. L. Hall, J. Math. Biol. **4**, 327 (1977).
[19] U. Euteneuer and M. Schliwa, Nature (London) **310**, 58 (1984).
[20] D. Selmeczi, S. Mosler, P. H. Hagedorn, N. B. Larsen, and H. Flyvbjerg, Biophys. J. **89**, 912 (2005).
[21] D. Selmeczi, L. Li, L. I. I. Pedersen, S. F. Nørrelykke, P. H. Hagedorn, S. Mosler, N. B. Larsen, E. C. Cox, and H. Flyvbjerg, Eur. Phys. J. Spec. Top. **157**, 1 (2008).
[22] L. Li, E. C. Cox, and H. Flyvbjerg (submitted 2011).
[23] L. Li, S. F. Nørrelykke, and E. C. Cox, PLoS ONE **3**, e2093 (2008).
[24] E. A. Codling, M. J. Plank, and S. Benhamou, J. R. Soc. Interface **5**, 813 (2008).
[25] E. Schwartz and J. Smith, Management Sci. **46**, 893 (2000).
[26] A. J. W. te Velthuis, J. W. J. Kerssemakers, J. Lipfert, and N. H. Dekker, Biophys. J. **99**, 1292 (2010).
[27] J. F. Beausang, C. Zurla, L. Finzi, L. Sullivan, and P. C. Nelson, Am. J. Phys. **75**, 520 (2007).
[28] W. H. Press, S. A. Teukolsky, W. T. Vetterling, and B. P. Flannery, *Numerical Recipes in FORTRAN: The Art of Scientific Computing*, 2nd ed. (Cambridge University Press, New York, 1992).
[29] R. Mannella, Stochastic Processes Phys. Chem. Biol. 353 (2000).